PEM Fuel Cell Stack Model Development for Real-Time Simulation Applications

Jee-Hoon Jung, *Member, IEEE*, Shehab Ahmed, *Member, IEEE*, and Prasad Enjeti, *Fellow, IEEE*

Abstract—The increased integration of fuel cells with power electronics, critical loads, and control systems has prompted recent interest in accurate electrical terminal models of the polymer electrolyte membrane fuel cell. Advancement in computing technologies, particularly parallel computation techniques and various real-time simulation tools, has allowed the prototyping of novel apparatus to be investigated in a virtual system under a wide range of realistic conditions repeatedly, safely, and economically. This paper builds upon both advancements and provides a means of optimized model construction boosting the computation speeds for a fuel cell terminal model on a real-time simulator which can be used in a power hardware-in-the-loop application. An elaborate simulation model of the fuel cell stack system has been developed, and a significant improvement in the computation time has been achieved. The effectiveness of the proposed model developed on Opal RT's RT-LAB MATLAB/Simulink-based real-time engineering simulator is verified using the experimental results with a Ballard Nexa fuel cell stack system.

Index Terms—Dynamic model, fast computation, polymer electrolyte membrane (PEM) fuel cell, real-time simulation.

NOMENCLATURE

α_a	Anode transfer coefficient (1.0).
α_c	Cathode transfer coefficient (0.9).
α_m	Mass transfer coefficient (0.5).
ρ_{lx}	Density of layer x (in kilograms per cubic centimeters).
σ	Stefan–Boltzmann constant (5.67×10^{-8} W/m² · K⁴).
σ_c	Electrical conductivity of the electrode (per ohms centimeter).
ε_s	Emissivity of the fuel cell stack (0.9).
A_c	Cross-sectional area of the conductor (in square centimeters).
a_{120}	Electrode specific interfacial area (10^4 cm²).
A_{cell}	Area of the fuel cell membrane (110 cm²).

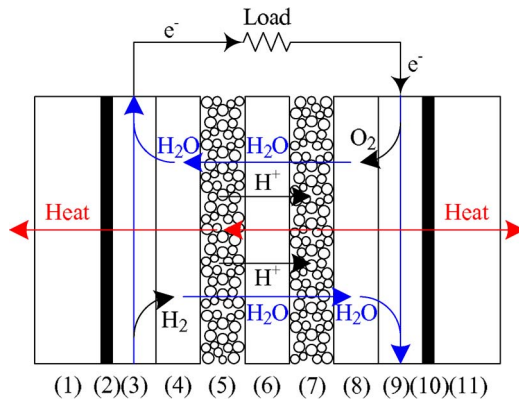|	
$A_{\text{cv},f}$	Effective area for forced convection (1.27 m²).
$A_{\text{cv},n}$	Effective area for natural convection (7.2×10^{-3} m²).
A_{lx}	Effective area of layer x (in square meters).
$C_{p,lx}$	Specific heat of layer x (in joules per gram kelvin).
$C_{p,x}$	Specific heat of material x (in joules per gram kelvin).
F	Faraday's constant (96 487 C).
G_f	Gibbs function in liquid form ($-228\,170$ J/mol).
h_f	Compensation coefficient for forced convection (0.01).
$h_{\text{cv},f}$	Forced convection coefficient (in watts per kilograms).
$h_{\text{cv},n}$	Natural convection coefficient (3.0 W/kg).
$H_{x,y}$	Enthalpy of x (material) as y (input/output; in joules per seconds).
i	Fuel cell output current density (in amperes per square centimeters).
I_s	Total stack current (in amperes).
i_{xr}	Exchange current density in x (h: H_2, o: O_2; in amperes per square centimeters).
L_c	Length of the conductor (in centimeters).
$m_{x,y}$	Mass flow rate of x (material) as y (in/out) (in grams per seconds).
M_{xg}	Mole fraction of x in the gas phase (H_2: 1, O_2: 0.21).
M_x	Molecule mass number of x (H_2: 0.002, H_2O: 0.018, N_2: 0.028, O_2: 0.032 kg/mol).
n_e	Number of electrons transferred per mol of reactant consumed (4).
n_x	Mol number of electrons per mol of x (H_2: 2, O_2: 4).
N_{cell}	Number of cells (47).
P_{tg}	Total gas pressure (in atmosphere).
Q_{lxR}	Heat flow from layer x to the solid material.
Q_{lx}	Heat flow from layer x to the mixed material.
$Q_{\text{res},lx}$	Heat generated by the resistance in layer x.
R	Ideal gas constant (8.314 J/mol K).
R_c	Contact resistance (0.005 Ω).
S	Saturation coefficient (0.6×10^{-12}).
T_o	Operating temperature (in degrees Celsius).
t_p	Membrane thickness (1.83×10^{-2} cm).
$T_{c,\text{in}}$	Cathode inlet temperature (in degrees Celsius).
T_{ca}	Temperature in the catalyst layer (in degrees kelvin).
T_{co}	Average temperature in the flow field, gas diffusion layer, and catalyst layer (in degrees kelvin).
T_{lx}	Borderline temperature of layer x (in degrees kelvin).
t_{lx}	Thickness of layer x (in meters).
U_{lx}	Overall heat transfer coefficient for layer x.
V_c	Maximum possible cell potential (in volts).
V_s	Total stack voltage (in volts).
W_{cp}	Output air mass flow of the air compressor (SLPM).

Fig. 1.　Layer structure and electrochemical reactions of the PEM fuel cell.

I. INTRODUCTION

FUEL CELLS provide a high-efficiency clean alternative to today's power generation technologies. The polymer electrolyte membrane (PEM) fuel cell has gained some acceptance in medium-power commercial applications such as building backup power, grid tied distributed generation, and electric vehicles [1]. Fig. 1 shows a representation of the PEM fuel cell's structure and electrochemical reactions. New control strategies have been developed [2], [3] for fuel cell applications [4]–[11]. The PEM fuel cell's terminal conditions demand the use of power conditioning subsystems to interface the fuel cell to its load or to the grid [12]–[14]. Load variations require a dynamic replenishment of the air and fuel supply while properly maintaining cell humidity and rejecting heat. Thus, the development and testing of the fuel cell systems in a laboratory environment would benefit from replacing fuel cells with accurate dynamic models and hardware simulators of the complete PEM fuel cell.

One-dimensional models of thermal response and water management have been proposed for estimating the behavior of the PEM fuel cell layers [15]. Dynamic fuel cell models predicting a detailed internal performance using electrochemical reaction and thermal dynamic equations have been reported in [16]–[21]. Model validations with commercial fuel cell systems are reported in [22]–[24]. Computational fluid dynamic simulations have also been used to corroborate the developed models [25].

Dynamic models based on algebraic computations have been developed for PEM fuel cell simulation [26]–[31]. The effect of the ripple current was analyzed, and a nonlinear controller was developed, employing dynamic simulations of a fuel cell [32], [33]. The real-time simulation of the fuel cell dynamic models has been used to improve the fuel cell subsystems and dc–dc converters [34]–[36]. The voltage and thermal dynamic models of the PEM fuel cell layers were organized, and the mathematical equations for the computational software were proposed in [37]. Moreover, the electrical and mathematical models of a Nexa fuel cell stack system, which is one of the well-known PEM fuel cell systems, have been developed to emulate its operation. Different parameters were suggested for steady-state and dynamic operations [38], and a linearized fuel cell and dc–dc converter model was proposed [39]. Addition-
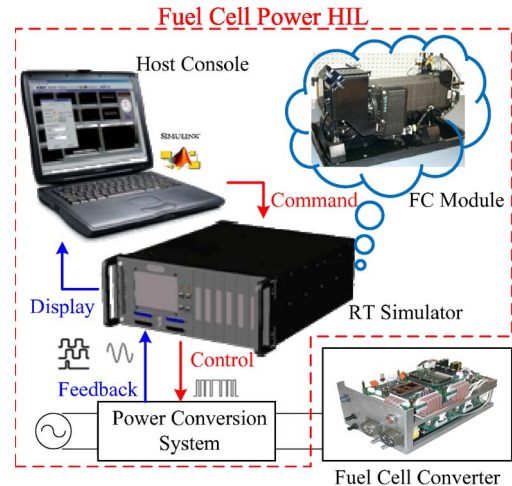

Fig. 2.　Conceptual schematic of fuel cell PHIL simulation.

ally, a simple circuit model was introduced to simulate the double layer charging effect [40]. A cell layer level dynamic model including electrical, fluid, and thermal multidomains was suggested [41], and a simplified model with parameter estimation and model prediction for a fuel cell's slow output transient was proposed [42].

Other fuel cell emulation systems previously presented in the literature do not consider model distribution onto more than one processor core in order to reduce the simulation time. Although this simplifies model development, it comes with its limitations. For example, the work in [34] used a single processor operating at 2.8 MHz as a real-time simulation system. In this system, the computation period was 1 ms. This system cannot support additional processes such as a dc/dc converter simulator or controller even if it operates at a switching frequency of 1 kHz, which is unrealistically low for submegawatt dc/dc converters. In addition, the work in [36] used an average PWM converter model as a fuel cell interface dc/dc converter. The converter model was limited to the averaged model instead of a full switched model to reduce the computation burden in real-time simulation. Thus, if a realistic dc/dc converter power hardware-in-the-loop (PHIL) system is to be developed, it is crucial that the simulation time is reduced.

In this paper, real-time simulation models are proposed for emulating a PEM fuel cell in the first step toward the development of a PHIL system that is similar to that shown in Fig. 2. Fuel cell systems are expensive, and the hydrogen supply system and auxiliary systems require additional engineering and safety precautions for laboratory testing. The real-time simulation based PHIL provides a fast, safe, and inexpensive way to accurately design and evaluate converters for fuel cell applications. The mathematical representation of the fuel cell electrochemistry was extracted from [35] and [37]. The mathematical equations of the terminal voltage, oxygen excess ratio (OER), and thermal dynamic models are programmed as simulation blocks in MATLAB Simulink. The paired t-test method is used for the statistical validation of the proposed simulation model compared to a Ballard Nexa fuel cell stack system. The proposed model dynamics of the major performance factors such as stack voltage, current, temperature, OER, and air mass
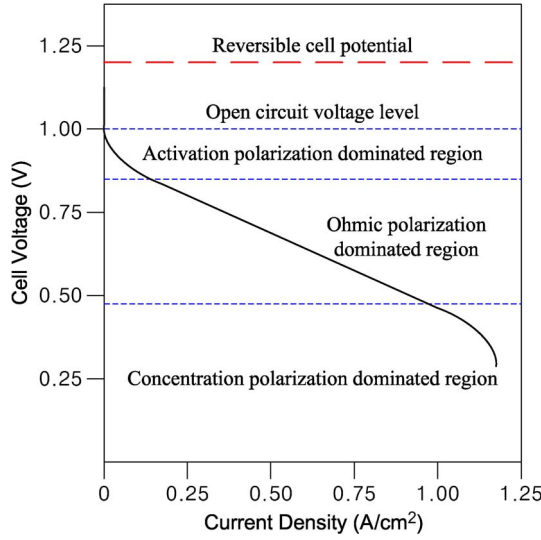
Fig. 3. Generalized polarization curve of a fuel cell.

flow of the air compressor are also verified. In order to optimize the simulation models for a real-time simulator, three methods will be proposed, which can boost the computation speed of real-time simulation. The proposed methods are minimizing algebraic calculation (MAC) and model separation (MS) and reducing the layer structure. They are generic in nature, and they can be implemented on any real-time simulator. The proposed models are tested and verified using the RT-LAB real-time engineering simulator from Opal-RT.

II. PEM FUEL CELL DYNAMIC MODEL

A. Voltage Model

Fig. 3 shows a generalized polarization curve which shows the typical voltage losses in a PEM fuel cell versus current density. Fuel cells provide a voltage that is dependent on operating conditions such as temperature, electrical load, and fuel and oxidant flow rates. The maximum possible cell potential V_c is the net output voltage given by (1), with the reversible cell potential V_{rv} and the irreversible potential V_{irv} [37]

$$V_c(i) = V_{rv} - V_{irv}. \qquad (1)$$

The reversible cell potential V_{rv} can be modeled as the Nernst voltage. To calculate the Nernst voltage as a reversible cell potential, the saturation pressure of water at temperature $T(°C)$, $p_{sat}(T)$ (SI), and the partial pressures of hydrogen pp_{H_2} and oxygen pp_{O_2} are used as follows [23], [28], [29]:

$$E_N = -\frac{G_f}{2F} - \frac{RT_o}{2F} \ln\left(\frac{p_{sat}(T_o)}{pp_{H_2} \cdot \sqrt{pp_{O_2}}}\right) \qquad (2)$$

$$\log_{10}[p_{sat}(T)] = -2.18 + 2.95 \times 10^{-2}T - 9.18 \times 10^5 T^2$$
$$+ 1.45 \times 10^7 T^3. \qquad (3)$$

For practical PEM fuel cell modules, which work under 100 °C, they are self-humidified in the cathode side, and they produce liquid water as the reaction product. Therefore, the
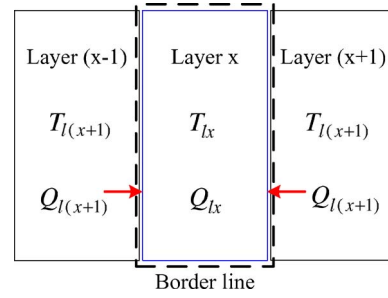
Fig. 4. General energy balance around layer x.

Nernst voltage (2) can be simplified by eliminating p_{sat}, as shown in the following:

$$E_N = 1.229 - 8.15 \times 10^{-4}(T - 298.15)$$
$$+ 4.308 \times 10^{-5}T \cdot \ln(pp_{H_2}\sqrt{pp_{O_2}}). \qquad (4)$$

The irreversible voltage loss is composed of the activation overpotential V_{act}, ohmic overpotential V_{ohm}, and concentration overpotential V_{con} in

$$V_{irv} = -V_{act} + V_{ohm} + V_{con}. \qquad (5)$$

The activation losses at the anode and cathode of the catalyst layer can be expressed as the Tafel equation [37]

$$V_{act} = \frac{RT_{ca}}{\alpha_c F}\left[\frac{\alpha_c}{\alpha_a + \alpha_c} \ln\left(\frac{\gamma}{i_{hr}M_{H_2g}}\right) - \ln\left(\frac{-\gamma}{i_{or}M_{O_2g}}\right)\right] \qquad (6)$$

where $\gamma = i[a_{120}(1 - S)P_{tg}]^{-1}$. The transport resistance of the charge particles (electrons and ions) results in a voltage loss for fuel cells, called ohmic loss in (7) [28], [37], where σ_m is the conductivity profile of the membrane and $\Delta\lambda$ is the variation of the water content, respectively

$$V_{ohm} = i\left[\sum_j R_{c,j} + \sum_k \frac{L_{c,k}}{\sigma_{c,k}A_{c,k}} + \int_0^{t_p} \frac{dz}{\sigma_m(\Delta\lambda(z))}\right]. \qquad (7)$$

The concentration loss caused by the convective and diffusive mass transport losses can be expressed by the Butler–Volmer equation in (8) [37], where $\bar{i}_L$ is the average limiting current density

$$V_{con} = \begin{cases} \frac{RT_{co}}{n_e F}\left(1 + \frac{1}{\alpha_m}\right)\ln\left(\frac{\bar{i}_L}{\bar{i}_L - i}\right), & i < \bar{i}_L \\ 0, & i \geq \bar{i}_L. \end{cases} \qquad (8)$$

B. Thermal Layer Model

To precisely predict the rates of electrochemical reaction and charge transport, the temperature and heat distribution need to be accurately determined. Solving for the heat transfer in the PEM fuel cell layers is a challenge because convective, radiative, and conductive heat transfers all exist [35]. The entropic heat is generated at two layers in unequal amounts. Fig. 4 shows a general energy balance around layer x. The proposed heat transfer model ignores the variation of entropy in

TABLE I
MATERIAL PROPERTIES OF THE CELL LAYERS

Fuel Cell Layer	Material	Thickness (m)	Density (kg/m^2)	Thermal Conductivity ($W/m \cdot K$)	Specific Heat Capacity ($J/kg \cdot K$)	Effective Area (m^2)
Coolant channel	Stainless	0.001	1400	30	935	0.15
Gasket	Cond. rubber	0.001	1400	1.26	1000	0.11
Flow field plate	Polycarbonate	0.001	1400	52	935	0.09
Diffusion layer		0.0004	2000	65	840	0.09
Catalyst layer		0.000065	387	0.2	770	0.09
Membrane	Nafion	0.000183	1976	0.21	1100	0.11

each layer and the thermal mass of the gas and liquid mixture to simplify its calculation. The general energy balance for a fuel cell layer x can be written in (9)[37], where m_{lx} is the thermal mass of layer x

$$m_{lx}\frac{dT_{lx}}{dt} = Q_{l(x-1)} + Q_{l(x+1)} \tag{9}$$

$$m_{lx} = \rho_{lx} A_{lx} t_{lx} C_{p,lx}. \tag{10}$$

Assuming that the temperature is uniformly distributed in the layer, each heat flow can be expressed in

$$Q_{l(x-1)} = U_{l(x-1)} A_{l(x-1)} \left(T_{l(x-1)} - T_{lx}\right)$$

$$Q_{l(x+1)} = U_{l(x+1)} A_{l(x+1)} \left(T_{l(x+1)} - T_{lx}\right). \tag{11}$$

The PEM fuel cell described in Fig. 1 is composed of the following 11 layers [35], [37]:

Layer 1: coolant channel;
Layer 2: gasket of the anode;
Layer 3: flow field plate of the anode;
Layer 4: gas diffusion layer of the anode;
Layer 5: catalyst layer of the anode;
Layer 6: membrane;
Layer 7: catalyst layer of the cathode;
Layer 8: gas diffusion layer of the cathode;
Layer 9: flow field plate of the cathode;
Layer 10: gasket of the cathode;
Layer 11: coolant channel.

Table I shows the parameters of the fuel cell layers used in the simulation. The effective area of all cell layers is 0.011 m². These parameters are obtained from [35] and [37] and from the data sheets of a fuel cell power module made by Ballard Power Systems. The governing equations for the heat transfer of each layer are as follows.

1) *Coolant channel:*

$$m_{l1}\frac{dT_{l1}}{dt} = Q_{cv} + Q_{rad} + Q_{l2} \tag{12}$$

where Q_{cv} is the heat flow by forced and natural convection and Q_{rad} is the heat flow by radiation, respectively. They are represented as (13) and (15)

$$Q_{cv} = (h_{cv,n} A_{cv,n} + h_{cv,f} A_{cv,f})(T_{amb} - T_{l1}) \tag{13}$$

$$h_{cv,f} = h_{f1}(h_{f2} I_s)^{h_{f3}} \tag{14}$$

$$Q_{rad} = \sigma \varepsilon_s A_{l1} \left(T_{amb}^4 - T_{l1}^4\right). \tag{15}$$

2) *Gasket:*

$$m_{l2}\frac{dT_{l2}}{dt} = Q_{l1} + Q_{l3}. \tag{16}$$

3) *Flow field plate:*

$$m_{l3}\frac{dT_{l3}}{dt} = Q_{l2} + Q_{l2R} + Q_{l4} + Q_{l4R} + Q_{res,l3}. \tag{17}$$

4) *Gas diffusion layer:*

$$m_{l4}\frac{dT_{l4}}{dt} = Q_{l3} + Q_{l3R} + Q_{l5} + Q_{res,l4}. \tag{18}$$

5) *Catalyst layer:*

$$m_{l5}\frac{dT_{l5}}{dt} = Q_{l4} + Q_{l6} + Q_{int,l5} + Q_{res,l5} \tag{19}$$

where $Q_{int,l5}$ is the heat generation due to the electrochemical reaction and voltage overpotential given by

$$Q_{int,l5} = \left(-\frac{T_{l5}\Delta S}{n_e F} - V_{act}\right) i A_{l5}. \tag{20}$$

It is noted that $\Delta S = 0.104$ J/mol K at the anode and -326.36 J/mol K at the cathode. The difference in ΔS between the anode and cathode creates asymmetry in the thermal distribution within the fuel cell.

6) *Membrane:*

$$m_{l6}\frac{dT_{l6}}{dt} = Q_{l5} + Q_{l7} + Q_{res,l6}. \tag{21}$$

The heat generation term in the membrane consists of joule heating only.

III. CONSIDERATIONS FOR THE FUEL CELL STACK SYSTEM

In this section, the single-cell simulation model proposed in the previous sections will be extended to the fuel cell stack system under several considerations of stacking, limitations of oxygen and hydrogen mass flow, and OER. Fig. 5 shows the proposed simulation model structure of the fuel cell stack system, which is composed of a cell model, stack model, and stack-cell interface. The cell model calculates the terminal voltage and layer temperature of the fuel cell. The stack model computes the stack current, the air mass flow of an air compressor, and the OER of the fuel cell stack. The cell and stack values of the voltage, current, and temperature are transformed to each other by the stack-cell interface.
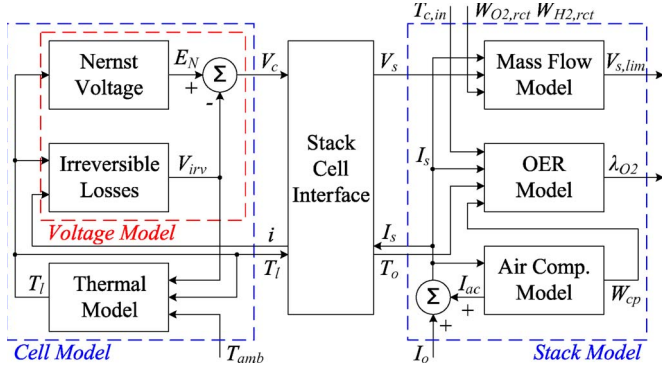
Fig. 5.   Proposed simulation model structure of the fuel cell stack system.

A. Stack Current, Voltage, and Temperature

The total stack current I_s, composed of the stack output current I_o and the subsystem current consumption I_{ss}, can be calculated using the cell current density i and the effective area of cell A_{cell} as in

$$I_s = I_o + I_{ss} = i A_{cell}. \tag{22}$$

The stack voltage can also be calculated using the number of cells N_{cell} under the consideration of the total stack resistance R_s and forward voltage drop of the stack diode V_f as follows:

$$V_s = V_c N_{cell} - R_s I_s - V_f \tag{23}$$

where $R_s = 0.11 \ \Omega$ and $V_f = 1.73$ V, respectively.

In the fuel cell stack, natural convection takes place in the cell's lateral walls. However, forced convection occurs in the cell's internal walls between each fuel cell due to the air cooler. This effect is already considered in (13) using different values of the effective cell areas for the convection. Forced convection occurs in all coolant layers (between adjacent fuel cells as well as at the outside layers). In this coolant layer, the heat flow by forced convection is greater than the conduction heat flow because of the higher temperature difference and larger effective area. The effect of the conduction heat transfer between two adjacent fuel cells is not more significant than the convection heat transfer. Therefore, the proposed single-cell temperature model can be expanded to a stack temperature model without serious temperature error. In addition, it can reduce the computation burden of real-time simulation.

B. Effects on Fuel and Air Mass Flow

The output power generated by the PEM fuel cell system is limited by the amount of supplied air (oxygen) and fuel (hydrogen). From the definition of current ($I = nF(dN/dt)$), the oxygen and hydrogen reaction rates (mass flows) are given by

$$W_{O_2,rct} = M_{O_2} \frac{N_{cell} I_s}{n_{O_2} F} \tag{24}$$

$$W_{H_2,rct} = M_{H_2} \frac{N_{cell} I_s}{n_{H_2} F}. \tag{25}$$

From (24) and (25), the total stack current I_s generated from the fuel cell stack is given by (26), considering the consumption of specific hydrogen and oxygen mass flows

$$I_s = \frac{n_{O_2} F}{N_{cell} M_{O_2}} W_{O_2,rct} = \frac{n_{H_2} F}{N_{cell} M_{H_2}} W_{H_2,rct}. \tag{26}$$

Therefore, the maximum stack current $I_{s,max}$ is limited by

$$I_{s,max} = \frac{F}{N_{cell}} \cdot \min \left[\frac{n_{O_2}}{M_{O_2}} W_{O_2,rct}, \frac{n_{H_2}}{M_{H_2}} W_{H_2,rct} \right]. \tag{27}$$

Since the maximum stack power $P_{s,max}$ is limited by $I_{s,max}$, the stack output voltage can be decreased by the limited amount of oxygen and/or hydrogen supplied from the air compressor and fuel tank. This can be expressed as follows:

$$P_{s,max} = N_{cell} V_c(i_{max}) I_{s,max} \tag{28}$$

$$V_{s,lim}(I_s) = \frac{P_{s,max}}{I_s} = N_{cell} V_c(i) \frac{I_{s,max}}{I_s} \tag{29}$$

where i_{max} is the maximum cell current density under limited air and/or fuel supplies. From (29), oxygen or hydrogen starvation implies a decrease in cell and stack voltage. This phenomenon is a serious danger to the fuel cell system because it can induce hot spots or burn-through on the surface of the membrane layer.

C. Effects of the OER

To prevent oxygen starvation in the membrane, the air compressor controller in the fuel cell system regulates the OER in the cathode by controlling the amount of oxygen mass flow from the air compressor to the inlet of the cathode [24]. The OER is defined by

$$\lambda_{O_2} = \frac{W_{O_2,in}}{W_{O_2,rct}}. \tag{30}$$

The oxygen reaction rate $W_{O2,rct}$ is obtained from (24), and the mass flow of O_2 through the inlet of the cathode $W_{O2,in}$ can be calculated as follows:

$$W_{O_2,in} = \gamma_{O_2,rct} W_{air,in} \tag{31}$$

where $W_{air,in}$ is the dry air flow in the cathode inlet and $\gamma_{O2,rct}$ is the molar mass relation between oxygen and dry air given by (32), where $M_{air,in}$ is the molar mass of dry air at the cathode inlet

$$\gamma_{O_2,rct} = \frac{M_{O_{2g}} M_{O_2}}{M_{air,in}} \tag{32}$$

$$M_{air,in} = M_{O_{2g}} M_{O_2} + M_{N_{2g}} M_{N_2}. \tag{33}$$

Equation (33) assumes that other gases in the air are negligible.

In addition, $W_{air,in}$ can be calculated from (34), where ω_{in} is the humidity ratio which is the relation between the masses of water vapor and dry air in the cathode inlet air, M_v is the water vapor molar mass, $\phi_{c,in}$ is the inlet air humidity, $p_{c,in}$ is

the cathode inlet pressure, and $p_{v,\text{in}}$ and $p_{d,\text{in}}$ are the partial pressures of water vapor and dry air, respectively

$$W_{\text{air,in}} = \frac{1}{1+\omega_{\text{in}}} W_{\text{in}} \tag{34}$$

$$\omega_{\text{in}} = \frac{M_v}{M_{\text{air,in}}} \cdot \frac{p_{v,\text{in}}(T_{c,\text{in}})}{p_{d,\text{in}}(T_{c,\text{in}})} \tag{35}$$

$$p_{c,\text{in}} = 1.0033 + (2.1 \times 10^{-3})W_{cp} - (475.7 \times 10^{-6})I_s \tag{36}$$

$$p_{v,\text{in}}(T) = \phi_{c,\text{in}} p_{\text{sat}}(T) \tag{37}$$

$$p_{d,\text{in}}(T) = p_{c,\text{in}} - p_{v,\text{in}}(T). \tag{38}$$

It is noted that (36) comes from an empirical testing reported in [24]. The cathode inlet air flow W_{in} can be calculated from (39), where M_{am} is the inlet air molar mass

$$W_{\text{in}} = \frac{W_{cp}}{22.4 \times 60} M_{am} \tag{39}$$

$$M_{am} = \frac{p_{d,\text{in}}(T_o)}{p_{c,\text{in}}} M_{\text{air,in}} + \frac{p_{v,\text{in}}(T_o)}{p_{c,\text{in}}} M_{\text{H}_2\text{O}}. \tag{40}$$

The higher OER consequently causes the higher output voltage of the fuel cell stack system. A high OER is induced from a high air mass flow of the air compressor. It increases the inlet pressure of the cathode, which is proportional to the partial pressure of O_2 (pp_{O2}). This high pp_{O2} increases the Nernst voltage E_N described in (2). Therefore, the stack output voltage will increase due to a high OER under the consumption of the same amount of oxygen and hydrogen.

D. Modeling of the Air Compressor

In the Nexa fuel cell system, the dynamics of the output air mass flow of the air compressor can be modeled as follows [24]:

$$W_{cp}(s) = \frac{0.1437s^2 + 2.217s + 8.544}{s^3 + 3.45s^2 + 7.324s + 5.745} V_{cr} \tag{41}$$

where V_{cr} is the air compressor's input voltage controlled by a Nexa control board, which can be expressed as in (42) using a curve fitting method from the experimental data

$$V_{cr} = 1.73 \times 10^{-3} I_s^3 - 0.128 I_s^2 + 3.62 I_s + 0.352. \tag{42}$$

The current consumption of the air compressor I_{ac} can be modeled with respect to the air mass flow of the compressor as in

$$I_{ac} = -2.43 \times 10^{-5} W_{cp}^3 + 4.22 \times 10^{-3} W_{cp}^2 - 0.174 W_{cp} + 3.83. \tag{43}$$

The power consumptions from other fuel cell subsystems, such as the control board and cooling fan, are included in I_{ac} since they are smaller than the power consumption of the air compressor ($I_{ss} \approx I_{ac}$).
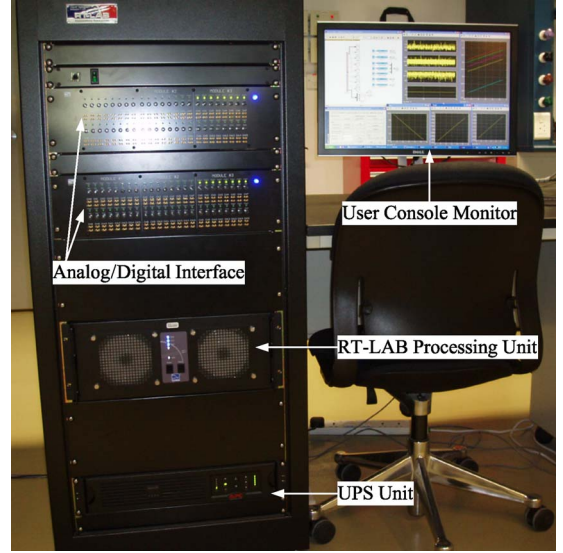

Fig. 6. Instrument photograph of the RT-LAB real-time simulator.

IV. FAST COMPUTATION METHODS FOR REAL-TIME SIMULATION

The terminal voltage, stack interface, and thermal dynamic models are implemented using MATLAB/Simulink. The Simulink models are compiled using the Opal-RT's RT-LAB real-time simulator. Fig. 6 shows the real-time simulation machine and its console monitor. The platform provides parallel computing hardware capability and accompanying transient solvers and component libraries. The optimal model construction for real-time simulation needs to take the simulator hardware architecture into consideration. In addition, the model structures should be simplified to reduce the computational burden. This section introduces the fuel cell base model development on the real-time simulator as well as the proposed approaches to reduce the model computation time. These approaches are the following: equation construction for MAC, model distribution for a multicore simulator, and reduced layer (RL) modeling for eliminating model redundancy.

A. Model Structure for Real-Time Simulation

The fuel cell's electrochemical equations show the strong correlation between the output voltage and layer temperatures. The cell voltage is a function of pressure, current, and temperature. The pressure and current are determined by the air and fuel supply as well as loading conditions. Temperature is dependent on the thermal dynamics and heat generations of the fuel cell layers as well as the cooling subsystem. In addition, the layer temperature is influenced by the irreversible voltage loss and cell current. The overall stack and console system and the dynamic simulation model of the real-time simulator based fuel cell stack system in Fig. 7 illustrate these interdependencies.

The overall dynamic simulation model in Fig. 7(a) is composed of two major types of blocks: dynamic system and monitoring/console system blocks. In Fig. 7(b), the dynamic
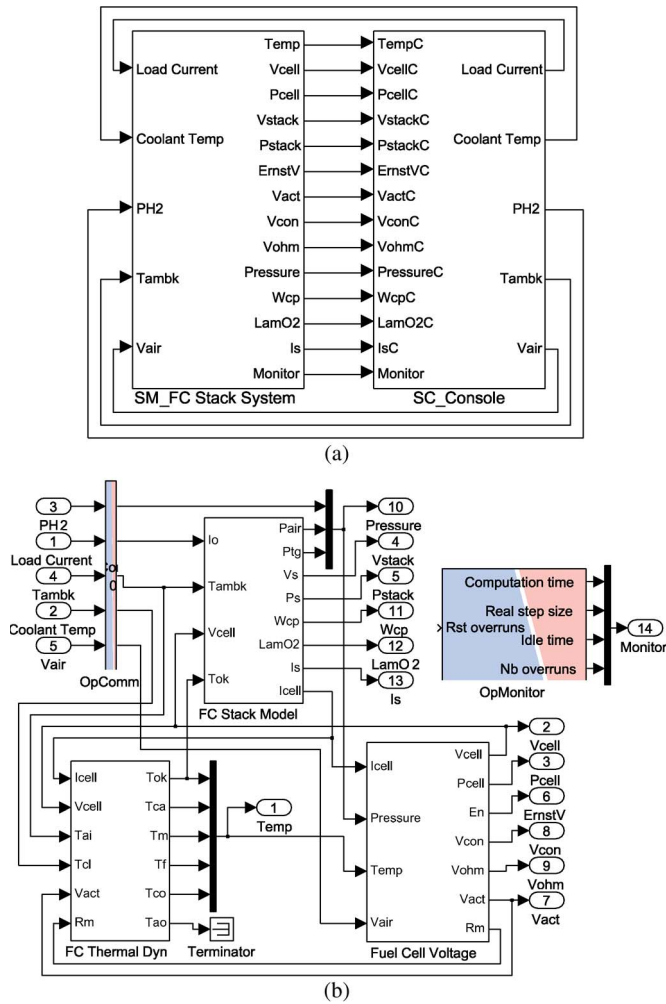
Fig. 7. PEM fuel cell dynamic model constructed by MATLAB Simulink. (a) Fuel cell stack and console system. (b) Fuel cell system dynamic model.

Fig. 8. Mathematical simulation model of the fuel cell terminal voltage.

Fig. 9. Thermal dynamic simulation model of the fuel cell system.

system blocks consist of thermal dynamic, cell voltage, and stack interface blocks. Additional OpComm and OpMonitor blocks are needed by RT-LAB. The OpComm block creates a real-time communication link between the model and simulator's input/output. The OpMonitor block adds real-time monitoring capability to the simulation.

Fig. 8 shows the mathematical simulation model of the fuel cell output voltage. This model is composed of the Nernst voltage block as the reversible voltage source and the activation loss block, ohmic loss block, and concentration loss block as the irreversible voltage losses. The input cell current and output cell voltage have range limitations because the cell voltage model provides meaningful results only under proper operating voltage and current values. Fig. 9 shows the thermal dynamic simulation model of a PEM fuel cell. It is composed of a thermal dynamic system block of cell layers and an air temperature block. The temperatures of the adjacent layers become the inputs of each block. Fig. 10 shows the stack interface model of the fuel cell system. This model calculates the OER, pressures, air mass flow of the air compressor, and total stack current. In addition, the stack interface model transforms the cell voltage to the stack voltage and the stack current to the cell current.
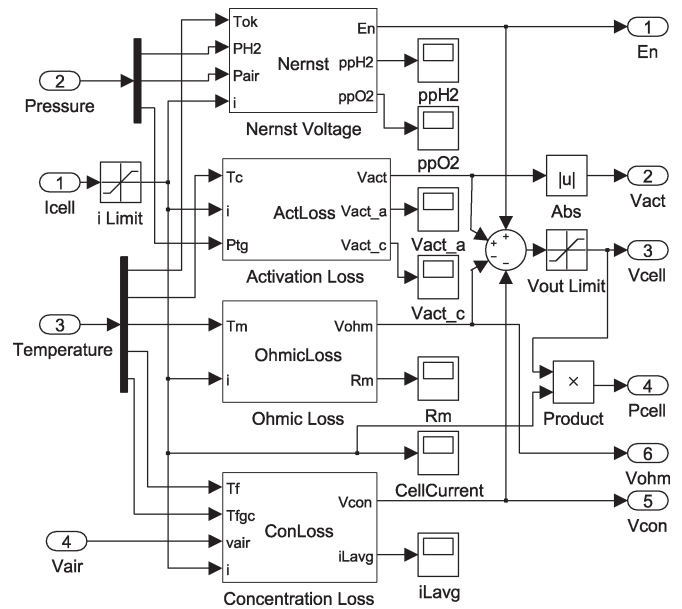
B. Model Construction for MAC

The real-time simulation environment has limitations of the simulator performance and computation time. The real-time simulation machine has fixed and limited processing power. The computation time is a more critical constraint because all computations should be completed within a fixed simulation time step. If not, overruns will cause errors to occur in the simulation, and they can propagate to the entire process. MAC is one method in enhancing the simulation performance. MAC is based on extracting the fixed parameters and coefficients from the model equations. Since the computational results of the fixed values are constant, they can be precalculated before the simulation process.

For example, the reversible voltage and all irreversible voltage losses can be simplified. Equation (8) has three variables: T_{co}, i, and $\bar{i}_L$. Other coefficients are constant and are
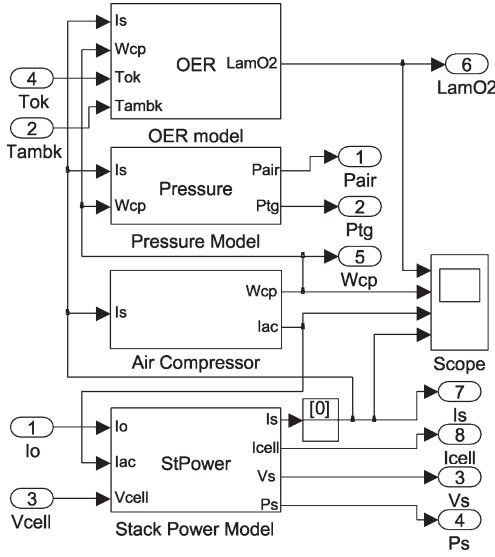
Fig. 10. Fuel cell stack interface model.

determined by the chemical reaction principles and physical PEM fuel cell characteristics. Therefore, (8) can be reformulated as follows:

$$V_{\mathrm{con}} = k_\alpha T_{co} \ln\left(\frac{\bar{i}_L}{\bar{i}_L - i}\right) \qquad (44)$$

where $k_a = R(n_e F)^{-1}(1 + \alpha_m^{-1})$. In addition, the heat transfer model of the fuel cell layers can be divided into constants and layer temperatures. From (10) and (11), the general energy balance between layers in (9) is reformulated as follows:

$$\frac{dT_{lx}}{dt} = k_{b1} T_{l(x-1)} + k_{b2} T_{l(x+1)} - (k_{b1} + k_{b2}) T_{lx} \qquad (45)$$

where

$$k_{b1} = \frac{U_{l(x-1)} A_{l(x-1)}}{m_{lx}}$$
$$k_{b2} = \frac{U_{l(x+1)} A_{l(x+1)}}{m_{lx}}. \qquad (46)$$

The MAC method can reduce the computational burden by the MACs in real-time simulation. However, the variations or modifications in the target fuel cell system will require updates to all of the precalculated values. Therefore, model development should take this into consideration to create a user-friendly model.

C. MS for a Multicore Simulator

The RT-LAB real-time simulator setup used in this paper has two Intel Core2Quad processors which have four cores, each operating at 2.5 GHz. Thus, the model computation speed can be improved if one makes use of the various processor cores. This is achieved by proper MS. The simulation models should be separated, so they only exchange priority signals which are state or state-derived between computation subsystems. Fig. 7(a) shows the conventional single structure of the fuel cell dynamic model and console. There is a single master block assigned to only one core for calculating the thermal dynamics
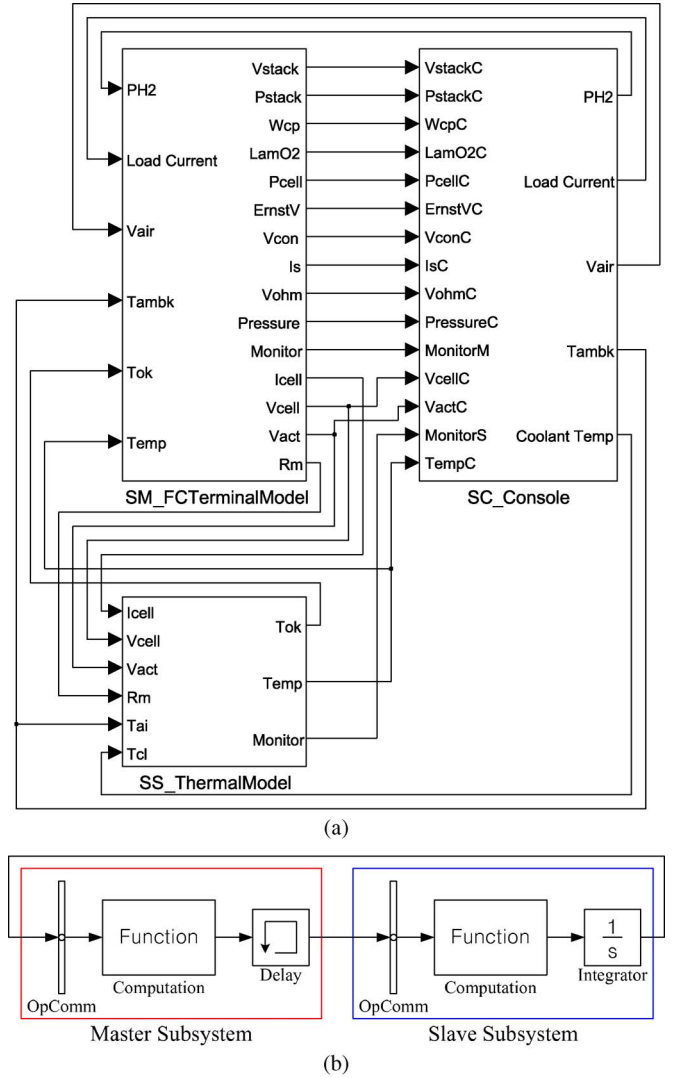

(a)

(b)

Fig. 11. Parallel computation of the simulation model. (a) Parallel model structure. (b) Fully parallel execution.

and voltage losses. Fig. 11(a) shows a parallel structure separating the fuel cell terminal block and thermal dynamic block. The fuel cell terminal block is composed of the cell voltage and stack interface models. By separating the model into master and slave subsystem blocks, the simulator can assign each model to different cores for parallel computing.

In order to maximize parallelism, the master and slave subsystems have to compute and send their outputs before they read their inputs within the same simulation step if the computation nodes exchange only the priority signals. The outputs are computed by migrating upstream until a dynamic state is found. If none is found, the simulation gives errors. Therefore, the state or state-derived signals have to be identified to enable the parallel computation of the subsystems. Fig. 11(b) shows the best structure for the parallel execution in the real-time simulator. A state can be defined as an output computed only from the preceding inputs or outputs. It means that the output blocks of the master and slave subsystems, which introduce states, have to be delayed. The output state of the thermal dynamic model is naturally connected to an integrator block. Therefore, the thermal dynamic model is suitable as a slave subsystem.

Unfortunately, in some cases, MS will not provide the parallel execution needed in real-time simulation. For example, a gain block does not produce a state because its output at an arbitrary time step depends on its input at the same time step. By using the delay block, the feed-through signals can be converted to priority signals. It should also be noted that the delay blocks need to be handled with care since they can alter the model dynamics. The simulation results should be compared before and after to make sure that the impact of the delay block is acceptable. In the case of the proposed thermal dynamic model, the time constant of the thermal dynamics is a few minutes. Thus, the impact of the delay is not significant.

Only for a single stack fuel cell system, a real-time simulator using a single processor may be acceptable in emulating the slow dynamics of the fuel cell stack. However, in the case of model expansion to parallel or series connection of several FC stack systems and the accompanying balance of plant components and dc/dc converters in a PHIL configuration, a multicore simulator is required to reduce the computation times to acceptable levels. The limitations found in [34] and [36] support this conclusion. The cost of a multicore multiprocessor system is not lower than the cost of a single-core single processor. However, multicore processors are widely used in today's computing environments.

The RT-LAB real-time simulator used in this paper has two Core2Quad processors. However, only two cores of a single processor were used to achieve the reductions in simulation time. If the real-time simulation model of the fuel cell is distributed onto three or more cores for parallel computation, the computation time is expected to decrease further. However, the decrease in time is not a direct linear relation, and it will have two main tradeoffs, namely, model complexity and model accuracy. The distributed model will require additional complexities to eliminate the algebraic loops and to distribute the functional blocks for parallel computation using more than two cores. In addition, the effects of the signal delay should be considered in the dynamics of such a model. These delays are caused by memory blocks and filters which are needed to synchronize the feedback signals between the submodels. Increasing the number of delay blocks to allow additional parallel computation is detrimental to the accuracy of the model dynamics. Therefore, the model distribution for increased parallel computation should consider these tradeoffs in its application. Challenges, tradeoffs, and limits related to further model distribution using a real-time simulator are possible further areas of research.

It should also be noted that the calculation time is highly dependent on the degree of MS and distribution. If the computation burden of the simulation model is equally divided into several models that are, in turn, assigned to multiple cores, the total computation time is expected to be approximately divided by the number of cores used compared to the single-core case. However, if the model is not equally divided, the computation time will follow the calculation speed of the most complex one of the distributed models. Thus, it is safe to say that the minimum number of cores needed for a distributed real-time simulation is that which allows the complete system dynamics to be simulated with no loss in accuracy when the model is approximately equally separated.
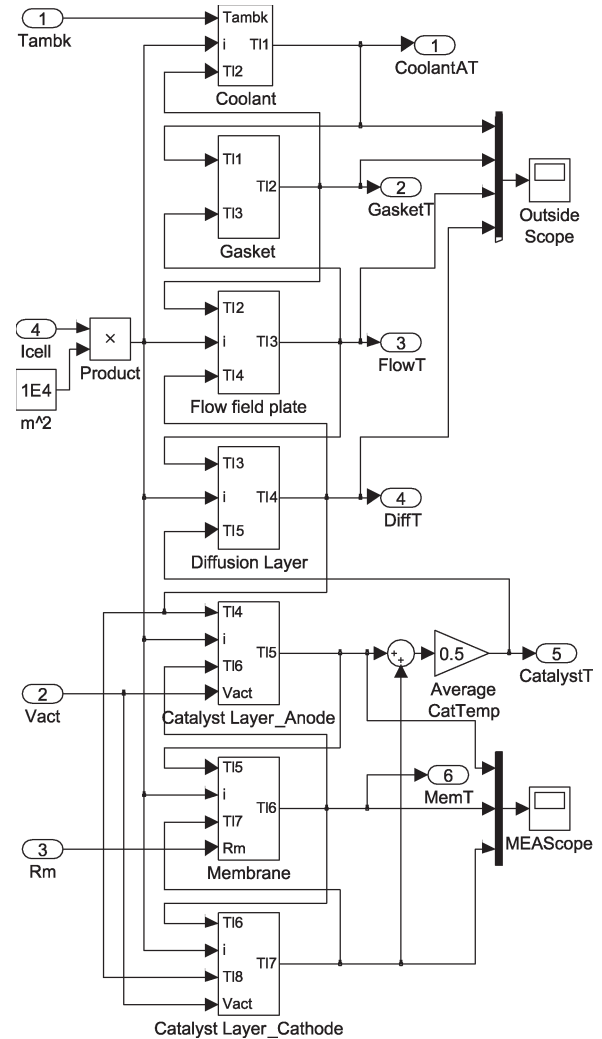

Fig. 12. RL structure of the simulation model.

D. RL Model of the PEM Fuel Cell

In Fig. 1, one can see that the anode and cathode layer structures of the PEM fuel cell are almost symmetric around a membrane. From (20), the difference between the anode and cathode layers is only the heat generation by the electrochemical reaction in the catalyst layer. The base model needs to compute all of the 11 thermal dynamic blocks within a single time step. If the model of cell layers is simplified using fuel cell symmetry, the computational burden can be reduced. Fig. 12 shows an RL structure of the simulation model. In Fig. 12, only seven blocks, instead of 11, are required to compute the fuel cell dynamics.

This RL model is generated using an approximation of the catalyst asymmetry between the anode and cathode. In Fig. 12, the feedback temperature of the gas diffusion layer is taken as the average temperature of the anode and cathode catalyst layers. This approximation induces slight errors in the calculation results of the layer temperatures. At a rated steady-state operation of the FC stack system, the dominant polarization loss is the ohmic loss. From (7), however, the ohmic loss has a little dependence on the operating temperature. Therefore, the slight temperature error caused by the RL approximation

can affect only the Nernst voltage. From (2), the new Nernst voltage due to the temperature error T_e caused by the RL approximation can be expressed as follows:

$$E'_N = -\frac{G_f}{2F} - \frac{R(T_o + T_e)}{2F} \ln \left(\frac{p_{\text{sat}}(T_o + T_e)}{pp_{H_2} \times \sqrt{pp_{O_2}}} \right) \quad (47)$$

where the saturation pressure of water at the operating temperature with an error can be approximately calculated using (3) as follows:

$$p_{\text{sat}}(T_o + T_e) \approx 10^{2.95 \times 10^{-2} T_e} \cdot P_{\text{sat}}(T_o). \quad (48)$$

From (48), the value of $p_{\text{sat}}(T_o + T_e)$ converges to $p_{\text{sat}}(T_o)$ with a small temperature error. Using (47) and (48), the cell voltage error caused by the temperature error can be estimated as shown in

$$E_N - E'_N = \Delta E_N \approx \frac{R}{2F} \ln \left(\frac{p_{\text{sat}}(T_o)}{pp_{H_2} \times \sqrt{pp_{O_2}}} \right) \cdot T_e. \quad (49)$$

From (49), the cell voltage error is almost linear with respect to the temperature error.

E. Advantages of the Proposed Methods in the View Point of Generality

The advantages of the proposed methods are the reduction of the computational burden in real-time simulation and the generic nature of the proposed algorithms, enabling their application on any commercial real-time simulator. The previous sections detailed how the proposed methods can reduce the simulation time step, introducing only a minor approximation. The proposed MAC method and RL model do not depend on specific technology and real-time simulator because their computational burden reduction schemes are based on general mathematical algorithms. The MS method is designed for multicore simulators. However, the multicore processing technology is widely used in general-purpose microprocessors. Another commercial real-time simulator (RTDS) supports parallel processing using multicore processors. Additionally, dSpace, which is a generic real-time simulator, also supports parallel processing. Consequently, the proposed fast computation methods in this paper are general algorithms, and they can be widely applied to any commercial real-time simulators.

V. RESULTS

In this section, the performance and validity of the proposed fuel cell dynamic model are discussed. The fuel cell output voltage and output power are illustrated according to the current density and operating temperature. The thermal dynamics and steady-state temperatures of the layers are presented. In addition, the static and dynamic simulation results of the proposed model are verified using the experimental data of the Ballard Nexa fuel cell stack system. The proposed fast computation methods (MAC, MS, and RL) are also verified by simulation results using the RT-LAB real-time simulator.
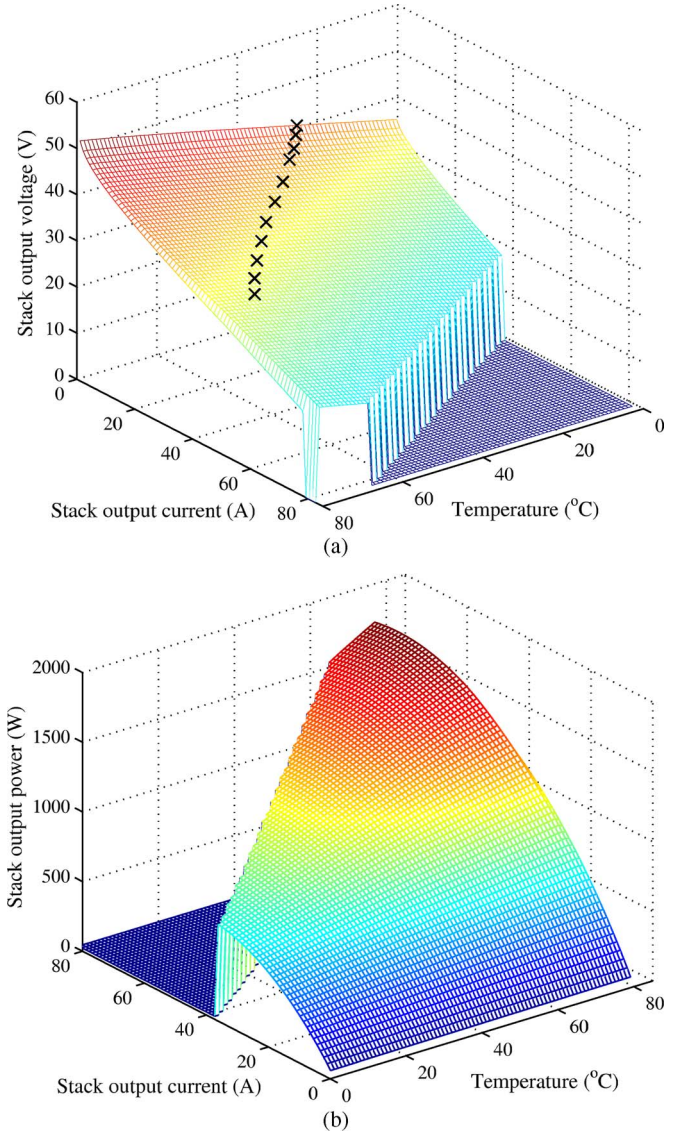

Fig. 13. Output characteristics of the fuel cell stack terminal voltage model. (a) Output voltage with experimental data. (b) Output power.

A. Model Characteristics

Fig. 13 shows the stack output voltage and power of the terminal voltage and stack interface models. According to these models, the stack output voltage changes for varying operating temperature and stack current. The stack voltage linearly increases when increasing the operating temperature and decreases proportionally to the stack output current. The stack output power shows a variation that is similar to the output voltage, and it has the maximum value around the highest current and temperature region. In Fig. 13, however, there are steeply collapsed regions of the stack output voltage and power because the proposed model considers the limitation of the stack voltage of the Nexa fuel cell system, which must be higher than 18 V.

Fig. 14 shows the temperature graphs of the fuel cell layers. Fig. 14(a) shows the transient thermal performance of the coolant, catalyst, and membrane layers evolving over 20 min. The initial cell temperature was set to 25 °C, and the load
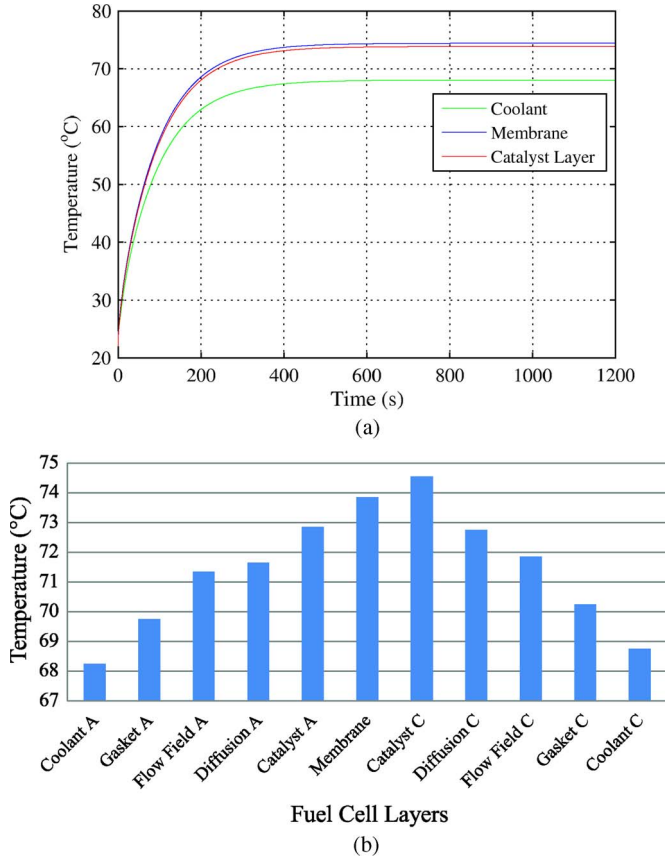
Fig. 15. Instrument photograph of the Nexa Ballard fuel cell stack system.

Fig. 14. Temperature in the cell layers 20 min into the simulation. (a) Temperature dynamic graph. (b) Temperature results of the layers.

Fig. 16. Paired *t*-test result of the stack voltage model.

current was assigned at 40 A. Fig. 14(b) shows the temperatures in all layers 20 min into the simulation. Characters A and C represent the anode and cathode, respectively. The cathode catalyst has the highest temperature because of a high ΔS in (20). The temperature difference between the conventional and RL models did not exceed 0.26 °C.

If some of the fuel cell parameters used in the model are inaccurate, errors will be introduced in the simulation results. In addition, inaccurate parameters in the voltage model can propagate computational errors to the thermal layer model and vice versa. Therefore, a calibration for unknown or inaccurate parameters is required using the experimental data of the target fuel cell system. Parameter adjustments can be achieved using the trial-and-error method from an initial parameter value, or one can use estimation algorithms for specific unknown parameters in the fuel cell system [43].

B. Model Validation Test

The validation of the proposed fuel cell stack dynamic simulation model was done using the experimental data with the 1.2-kW Nexa Ballard fuel cell stack system shown in Fig. 15. In Fig. 13(a), the experimental data (cross) are laid on the 3-D surface of the simulated voltage curve. In addition to the visual inspection of the data, a mathematical approach was also used. The paired *t*-test procedure is used to compute the mean difference between two populations when one believes that some dependence exists [44]. The paired *t*-test was carried out using
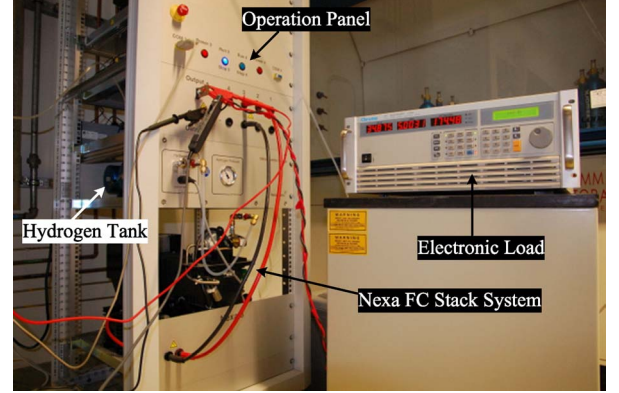
the statistical software MINITAB. Fig. 16 shows the paired *t*-test result of the static response of the stack terminal voltage shown in Fig. 13(a). Fig. 16 means that the difference between the two data sets can be ignored with a 95% confidence level.

Fig. 17 shows the comparison between the experimental data and the simulation model response in the stack current, air mass flow of the air compressor, OER, and stack voltage. The good agreement in transient dynamics and steady-state values between the simulation model and experimental results holds for all of the fuel cell's performance factors. Fig. 18 shows the comparison of the thermal dynamic data with respect to loads of 10 and 30 A evolving over 20 min. The ambient temperature in this case was 27.5 °C, which was also used as the initial temperature in the simulation. In Fig. 18, the proposed thermal dynamic model of the fuel cell layers accurately calculates the experimental temperature data for various load conditions.

For a detailed validation of the model accuracy, another error analysis has been carried out using the mean relative error (MRE) criterion [24] as follows:

$$\text{MRE}(\%) = 100 \times \frac{1}{N} \sum_{j=1}^{N} \left| \frac{D_j^e - D_j^s}{D_j^e} \right| \tag{50}$$

where D_e^j and D_s^j represent the experimental and simulated data sets, respectively, and N is the number of samples. Using (50), the MRE criterion is applied to the dynamic responses of the stack voltage, the OER, and the thermal dynamic responses. As a result, the relative mean errors of the stack voltage and
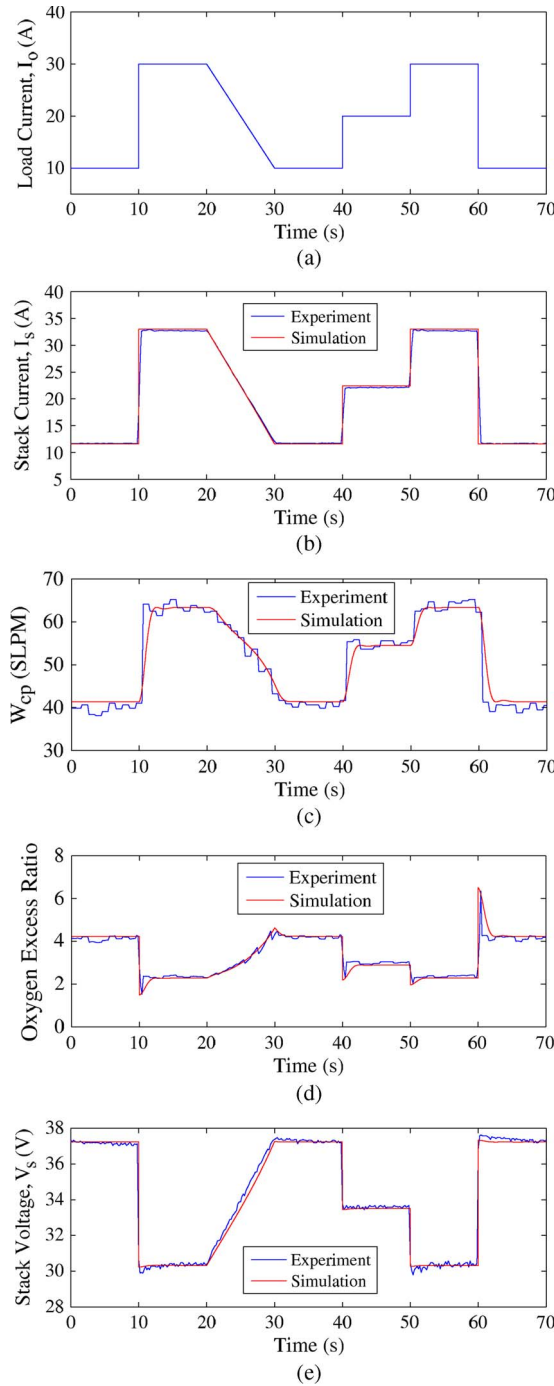
Fig. 17. Comparison between the experimental data and the simulation model response. (a) Load current. (b) Stack current. (c) Air mass flow of the air compressor. (d) OER. (e) Stack voltage.
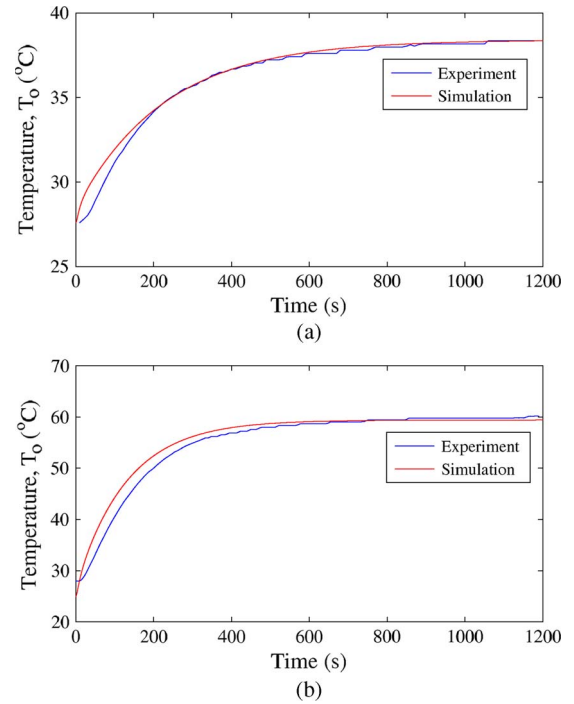

Fig. 18. Comparison of the thermal dynamic data with respect to the load conditions. (a) 10-A load. (b) 30-A load.
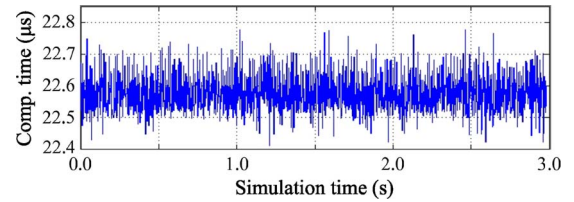

Fig. 19. Simulation computation time of the base model.

the air-flow stoichiometry and the stack current measured by the system controller. The controller's measurement error of the OER can be higher than other variables because it is based on the value of the air-flow stoichiometry calculated from other variables. However, the maximum error of the OER is bounded because all other variables which participate in the calculation of the OER as linear combination terms are bounded. Therefore, the controller's measurement error is acceptable in the proposed PEM fuel cell model.

C. Improved Computation Speed

Fig. 19 shows the real-time simulation computation time of the base fuel cell model. The computations of the base model were completed in an average of 22.6 μs. Fig. 20 shows the improvement in computation time using the proposed fast computation methods. Fig. 20(a) shows the computation time when the model is modified using the MAC method. The results show a 38% reduction in computation time using this method. Fig. 20(b) and (c) shows the computation time reduction for a model altered using the MS method for the multicore simulator. The master block which computes the voltage loss model requires 5.9 μs, and the slave block which computes the thermal dynamic model of the fuel cell layers consumes 0.9 μs. The RL

OER are 0.73% and 2.31%, respectively. In addition, the errors of the thermal dynamics at 10- and 30-A load conditions are calculated as 3.83% and 6.56%, respectively.

All of the measurements of the stack current, air mass flow, OER, and stack voltage were carried out using the monitoring functions of the system controller. In order to calculate the OER, the oxygen mass flow through the inlet could be obtained using a monitored value of the air-flow stoichiometry calculated from the air mass flow and the current draw. The experimental data of the OER could be calculated using (24) and (30), with
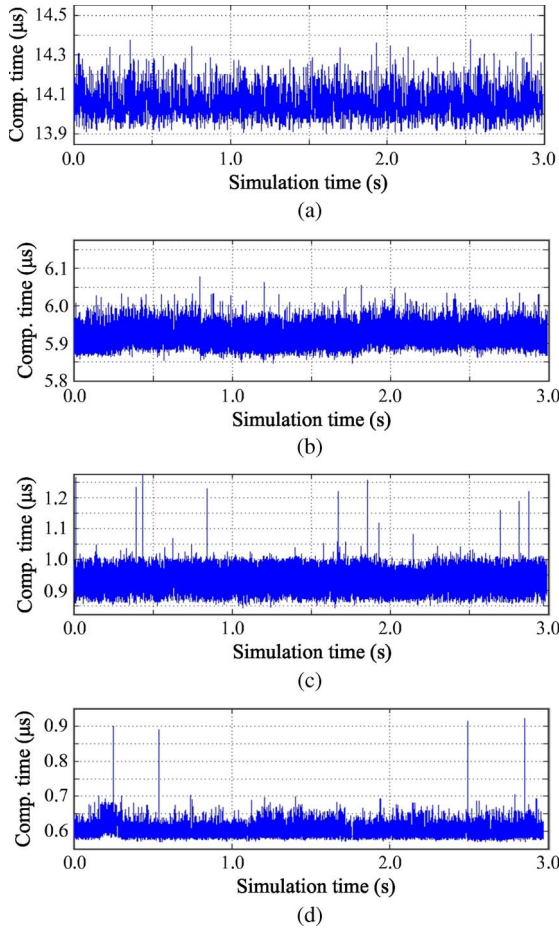
Fig. 20. Improved computation speed using the proposed methods. (a) MAC method. (b) MS master model. (c) MS slave model. (d) RL slave model.

method saves an additional 33% of the computation time of the thermal dynamic layer model, as shown in Fig. 20(d).

Fig. 21 shows the performance of a complete simulation model, including all of the proposed methods of computation time reduction. The time consumptions of the voltage loss and thermal dynamic layer models are 3.5 and 0.6 μs, respectively. Consequently, the improvement in computation time brought about by the proposed model development approach is on the order of 82%. Table II shows the computation times of the proposed methods.

VI. CONCLUSION

A computationally efficient electrical and thermal dynamic model of the PEM fuel cell for real-time simulation has been presented. The proposed model includes the electrical voltage and thermal dynamics of individual fuel cell layers. In addition, the stack voltage and current are calculated in emulating the fuel cell stack system, considering several effects such as fuel and air supplies and the OER. By MACs, by performing MS, and by utilizing the fuel cell structure symmetry (RL), the proposed fuel cell model's execution time is improved. The proposed model was tested and verified using the RT-LAB real-time simulator and the Ballard Nexa fuel cell system. An 82% improvement in computation speed over the base model was
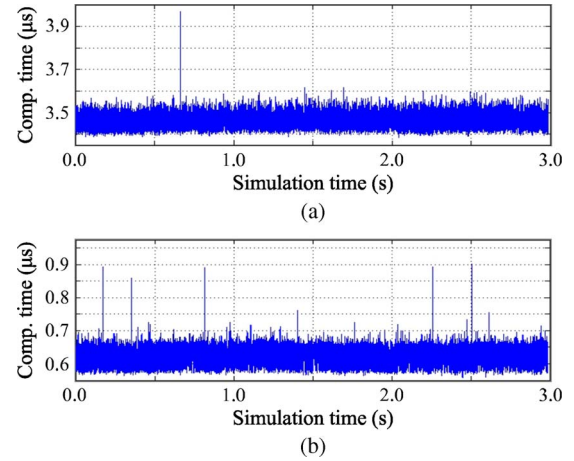

Fig. 21. Computational time consumption of the complete model. (a) Master voltage model. (b) Slave thermal dynamic model.

TABLE II
COMPUTATION TIME OF THE PROPOSED METHODS

Model	Base	MAC	MS	SL	Complete
Serial	22.6 μs	14.1 μs	-	-	-
P. Master	-	-	5.9 μs	5.9 μs	3.5 μs
P. Slave	-	-	0.9 μs	0.6 μs	0.6 μs

achieved. In addition, the static output values and transient dynamics of the proposed model have also been verified using the experimental data both visually and using the paired t-test approach. The proposed fuel cell model accurately and quickly calculates the system dynamics in real time, and it can be used for the fast prototyping of a fuel cell system.

Extending the proposed model to a real-time model based controller for emulating the fuel cell stack system is a natural continuation of this paper. This paper is the first step in the development of a fuel cell based PHIL architecture.

REFERENCES

[1] B. D. Solomon and A. Banerjee, "A global survey of hydrogen energy research, development and policy," *Energy Policy*, vol. 34, no. 7, pp. 781–792, May 2006.

[2] M. Tekin, D. Hissel, M.-C. Pera, and J. Kauffmann, "Energy-management strategy for embedded fuel-cell systems using fuzzy logic," *IEEE Trans. Ind. Electron.*, vol. 54, no. 1, pp. 595–603, Feb. 2007.

[3] C. A. Ramos-Paja, C. Bordons, A. Romero, R. Giral, and L. Martinez-Salamero, "Minimum fuel consumption strategy for PEM fuel cells," *IEEE Trans. Ind. Electron.*, vol. 56, no. 3, pp. 685–696, Mar. 2009.

[4] P. Thounthong, S. Rael, and B. Davat, "Control strategy of fuel cell and supercapacitors association for a distributed generation system," *IEEE Trans. Ind. Electron.*, vol. 54, no. 6, pp. 3225–3233, Dec. 2007.

[5] M. Todorovic, J. Palma, and P. Enjeti, "Design of a wide input range dc–dc converter with a robust power control scheme suitable for fuel cell power conversion," *IEEE Trans. Ind. Electron.*, vol. 55, no. 3, pp. 1247–1255, Mar. 2008.

[6] T. Haimin, J. Duarte, and M. Hendrix, "Line-interactive UPS using a fuel cell as the primary source," *IEEE Trans. Ind. Electron.*, vol. 55, no. 8, pp. 3012–3021, Aug. 2008.

[7] K. Jin, X. Ruan, M. Yang, and M. Xu, "A hybrid fuel cell power system," *IEEE Trans. Ind. Electron.*, vol. 56, no. 4, pp. 1212–1222, Apr. 2009.

[8] J. Kwon, E. Kim, B. Kwon, and K. Nam, "High efficient fuel cell power conditioning system with input current ripple reduction," *IEEE Trans. Ind. Electron.*, vol. 56, no. 3, pp. 826–834, Mar. 2009.

[9] L. Palma, M. Todorovic, and P. Enjeti, "Analysis of common-mode voltage in utility-interactive fuel cell power conditioners," *IEEE Trans. Ind. Electron.*, vol. 56, no. 1, pp. 20–27, Jan. 2009.

[10] M. Nymand and M. A. E. Andersen, "High-efficiency isolated boost dc/dc converter for high-power low-voltage fuel-cell applications," *IEEE Trans. Ind. Electron.*, vol. 57, no. 2, pp. 505–514, Feb. 2010.

[11] W. Jiang and B. Fahimi, "Active current sharing and source management in fuel cell-battery hybrid power system," *IEEE Trans. Ind. Electron.*, vol. 57, no. 2, pp. 752–761, Feb. 2010.

[12] J. Hall and R. Kerr, "Innovation dynamics and environmental technologies: The emergence of fuel cell technology," *J. Cleaner Prod.*, vol. 11, no. 4, pp. 459–471, Jun. 2003.

[13] X. Huang, Z. Zhang, and J. Jiang, "Fuel cell technology for distributed generation: An overview," in *Proc. IEEE Int. Symp. Ind. Electron.*, 2006, vol. 2, pp. 1613–1618.

[14] A. Averberg, K. R. Meyer, C. Q. Nguyen, and A. Mertens, "A survey of converter topologies for fuel cells in the kW range," in *Proc. IEEE Energy 2030 Conf.*, Nov. 2008, vol. 1, pp. 1–7.

[15] A. Rowe and X. Li, "Mathematical modeling of proton exchange membrane fuel cells," *J. Power Sources*, vol. 102, no. 1/2, pp. 82–96, Dec. 2001.

[16] J. M. Correa, F. A. Farret, L. N. Canha, and M. G. Simoes, "An electrochemical-based fuel-cell model suitable for electrical engineering automation approach," *IEEE Trans. Ind. Electron.*, vol. 51, no. 5, pp. 1103–1112, Oct. 2004.

[17] S. Pasricha and S. R. Shaw, "A dynamic PEM fuel cell model," *IEEE Trans. Energy Convers.*, vol. 21, no. 2, pp. 484–490, Jun. 2006.

[18] Z. Zhang, X. Huang, J. Jiang, and B. Wu, "An improved dynamic model considering effects of temperature and equivalent internal resistance for PEM fuel cell power modules," *J. Power Sources*, vol. 161, no. 2, pp. 1062–1068, Oct. 2006.

[19] A. J. del Real, A. Arce, and C. Bordons, "Development and experimental validation of a PEM fuel cell dynamic model," *J. Power Sources*, vol. 173, no. 1, pp. 310–324, Nov. 2007.

[20] H. Wu, X. Li, and P. Berg, "Numerical analysis of dynamic processes in fully humidified PEM fuel cells," *Int. J. Hydrogen Energy*, vol. 32, no. 12, pp. 2022–2031, Aug. 2007.

[21] A. Gebregergis, P. Pillay, D. Bhattacharyya, and R. Rengaswemy, "Solid oxide fuel cell modeling," *IEEE Trans. Ind. Electron.*, vol. 56, no. 1, pp. 139–148, Jan. 2009.

[22] M. Radulescu, V. Ayel, O. Lottin, M. Feidt, B. Antoine, C. Moyne, D. L. Noc, and S. L. Doze, "Natural gas electric generator powered by polymer exchange membrane fuel cell: Numerical model and experimental results," *Energy Convers. Manage.*, vol. 49, no. 2, pp. 326–335, Feb. 2008.

[23] M. V. Moreira and G. E. da Silva, "A practical model for evaluating the performance of proton exchange membrane fuel cells," *Renew. Energy*, vol. 34, no. 7, pp. 1734–1741, Jul. 2009.

[24] C. Ramos-Paja, R. Giral, L. Martinez-Salamero, J. Romano, A. Romero, and G. Spagnuolo, "A PEM fuel cell model featuring oxygen excess ratio estimation and power electronics interaction," *IEEE Trans. Ind. Electron.*, vol. 57, no. 6, pp. 1914–1924, Jun. 2010.

[25] C. Siegel, "Review of computational heat and mass transfer modeling in polymer-electrolyte-membrane (PEM) fuel cells," *Energy*, vol. 33, no. 9, pp. 1331–1352, Sep. 2008.

[26] L.-Y. Chiu, B. Diong, and R. S. Gemmen, "An improved small-signal model of the dynamic behavior of PEM fuel cells," *IEEE Trans. Ind. Appl.*, vol. 40, no. 4, pp. 970–977, Jul./Aug. 2004.

[27] M. Uzunoglu and M. S. Alam, "Dynamic modeling, design, and simulation of a combined PEM fuel cell and ultracapacitor system for standalone residential applications," *IEEE Trans. Energy Convers.*, vol. 21, no. 3, pp. 767–775, Sep. 2006.

[28] D. M. Ali, "A simplified dynamic simulation model (prototype) for a stand-alone polymer electrolyte membrane (PEM) fuel cell stack," in *Proc. 12th Int. MEPCON*, Mar. 2008, vol. 1, pp. 480–485.

[29] M. Soltani and S. M. T. Bathaee, "A new dynamic model considering effects of temperature, pressure and internal resistance for PEM fuel cell power modules," in *Proc. 3rd Int. Conf. Elect. Utility Deregulation Restruct. Power Technol. (DRPT)*, Apr. 2008, vol. 1, pp. 2757–2762.

[30] S. Jemei, D. Hissel, M.-C. Pera, and J. Kauffmann, "A new modeling approach of embedded fuel-cell power generators based on artificial neural network," *IEEE Trans. Ind. Electron.*, vol. 55, no. 1, pp. 437–447, Jan. 2008.

[31] X. Kong and A. M. Khambadkone, "Modeling of a PEM fuel-cell stack for dynamic and steady-state operation using ANN-based submodels," *IEEE Trans. Ind. Electron.*, vol. 56, no. 12, pp. 4903–4914, Dec. 2009.

[32] R. S. Gemmen, "Analysis for the effect of inverter ripple current on fuel cell operating condition," *J. Fluids Eng.*, vol. 125, no. 3, pp. 576–585, May 2003.

[33] W. K. Na and B. Gou, "Feedback-linearization-based nonlinear control for PEM fuel cells," *IEEE Trans. Energy Convers.*, vol. 23, no. 1, pp. 179–190, Mar. 2008.

[34] M. Meiler, O. Schmid, M. Schudy, and E. P. Hofer, "Dynamic fuel cell stack model for real-time simulation based on system identification," *J. Power Sources*, vol. 176, no. 2, pp. 523–528, Feb. 2008.

[35] S.-Y. Choe, J.-W. Ahn, J.-G. Lee, and S.-H. Baek, "Dynamic simulator for a PEM fuel cell system with a PWM dc/dc converter," *IEEE Trans. Energy Convers.*, vol. 23, no. 2, pp. 669–680, Jun. 2008.

[36] J.-G. Lee, S.-Y. Choe, J.-W. Ahn, and S.-H. Baek, "Modelling and simulation of a polymer electrolyte membrane fuel cell system with a PWM dc/dc converter for stationary applications," *IET Power Electron.*, vol. 1, no. 3, pp. 305–317, Sep. 2008.

[37] C. Spiegel, *PEM Fuel Cell Modeling and Simulation Using MATLAB*. New York: Academic, 2008.

[38] U. Reggiani, L. Sandrolini, and G. L. G. Burbui, "Modelling a PEM fuel cell stack with a nonlinear equivalent circuit," *J. Power Sources*, vol. 165, no. 1, pp. 224–231, Feb. 2007.

[39] J. M. Andujar, F. Segura, and M. J. Vasallo, "A suitable model plant for control of the set fuel cell-dc/dc converter," *Renew. Energy*, vol. 33, no. 4, pp. 813–826, Apr. 2008.

[40] S. Lazarou, E. Pyrgioti, and A. T. Alexandridis, "A simple electric circuit model for proton exchange membrane fuel cells," *J. Power Sources*, vol. 190, no. 2, pp. 380–386, May 2009.

[41] F. Gao, B. Blunier, A. Miraoui, and A. El-Moudni, "Cell layer level generalized dynamic modeling of a PEMFC stack using VHDL-AMS language," *Int. J. Hydrogen Energy*, vol. 34, no. 13, pp. 5498–5521, Jul. 2009.

[42] H. Kim, C. Y. Cho, J. H. Nam, D. Shin, and T.-Y. Chung, "A simple dynamic model for polymer electrolyte membrane fuel cell (PEMFC) power modules: Parameter estimation and model prediction," *Int. J. Hydrogen Energy*, vol. 35, no. 8, pp. 3656–3663, Apr. 2010.

[43] B. Carnes and N. Djilali, "Systematic parameter estimation for PEM fuel cell models," *J. Power Sources*, vol. 144, no. 1, pp. 83–93, Jun. 2005.

[44] R. E. Walpole and R. H. Myers, *Probability and Statistics for Engineers and Scientists*, 5th ed. Englewood Cliffs, NJ: Prentice-Hall, 1993.

Jee-Hoon Jung (M'07) was born in Suwon, Korea, in 1977. He received the B.S., M.S., and Ph.D. degrees from the Department of Electronic and Electrical Engineering, Pohang University of Science and Technology, Pohang, Korea, in 2000, 2002, and 2006, respectively.

He was a Senior Research Engineer with the Digital Printing Division, Samsung Electronics Co., Ltd., Suwon, from 2006 to 2009. He was also a Postdoctoral Research Associate with the Electrical and Computer Engineering Department, Texas A&M University at Qatar, Doha, Qatar. He is currently a Senior Researcher with the New and Renewable Energy System Research Center, Smart Grid Research Division, Korea Electrotechnology Research Institute, Changwon, Korea. His research interests include dc–dc converters, switched mode power supplies, motor drives and diagnosis systems, digital control and signal processing algorithms, digitally controlled power electronics, power conversions for renewable energy, and real-time and power hardware-in-the-loop simulations of renewable energy sources. He is recently researching on power conversions for dc distribution systems.

Dr. Jung is a member of the IEEE Industrial Electronics Society, IEEE Power Electronics Society, and Korean Institute of Power Electronics.

Shehab Ahmed (M'07) received the B.Sc. degree in electrical engineering from Alexandria University, Alexandria, Egypt, in 1999 and the M.Sc. and Ph.D. degrees from the Department of Electrical and Computer Engineering, Texas A&M University, College Station, in 2000 and 2007, respectively.

From 2001 to 2007, he was with the Schlumberger Technology Corporation working on downhole mechatronic systems. He is currently an Assistant Professor with the Texas A&M University at Qatar, Doha, Qatar. His research interests include mechatronics, solid-state power conversion, electric machines, and drives.

Prasad Enjeti (M'85–SM'88–F'00) received the B.E. degree in electrical engineering from Osmania University, Hyderabad, India, in 1980, the M.Tech. degree in electrical engineering from the Indian Institute of Technology Kanpur, Kanpur, India, in 1982, and the Ph.D. degree in electrical engineering from Concordia University, Montreal, QC, Canada, in 1988.

In 1988, he was with the Department of Electrical Engineering, Texas A&M University, College Station, as an Assistant Professor, where he was promoted as an Associate Professor in 1994, he became a Full Professor in 1998, and he is the Lead Developer of the Power Electronics/Power Quality and Fuel Cell Power Conditioning Laboratories. He is actively involved in many projects with industries while engaged in teaching, research, and consulting in the area of power electronics, motor drives, power quality, and clean power utility interface issues. He is the holder of four U.S. patents, and he has licensed two new technologies to the industry so far. His current research interests include advanced converters for power supplies and motor drives; power quality issues; active power filter development; utility interface issues; advancing switching power supply designs and solutions to complex power management issues in the context of analog and mixed-signal applications; exploring alternative designs to meet the demands of high slew rate load currents at low output voltages; power conditioning systems for fuel cells, wind, and solar energy systems; and design of high-temperature power conversion systems with wideband gap semiconductor devices.

Dr. Enjeti is a Registered Professional Engineer in the State of Texas. He was the recipient of the select title Class of 2001 Texas A&M University Faculty Fellow Award for demonstrating an achievement of excellence in research, scholarship, and leadership in the field. He was the recipient of the IEEE Industry Applications Society (IAS) Second and Third Best Paper Awards in 1993, 1998, 1999, 2001, and 1996; the Second Best IEEE-IA Transactions Paper published in midyear 1994 to midyear 1995; and the IEEE IAS Magazine Prize Article Award in 1996. In 2000, he was elected as a fellow by the IEEE Fellows Committee for his contributions to the solutions of the utility interface problems in power electronic systems and harmonic mitigation. He directed a team of students to design and build a low-cost fuel cell inverter for residential applications, which won the 2001 Future Energy Challenge Award Grand Prize from the Department of Energy.